Self-Consistent Analysis of Strain-Compensated InGaN–AlGaN Quantum Wells for Lasers and Light-Emitting Diodes

Hongping Zhao, Ronald A. Arif, Yik-Khoon Ee, and Nelson Tansu

***Abstract*—Strain-compensated InGaN–AlGaN quantum wells (QW) are investigated as improved active regions for lasers and light emitting diodes. The strain-compensated QW structure consists of thin tensile-strained AlGaN barriers surrounding the InGaN QW. The band structure was calculated by using a self-consistent 6-band $k \cdot p$ formalism, taking into account valence band mixing, strain effect, spontaneous and piezoelectric polarizations, as well as the carrier screening effect. The spontaneous emission and gain properties were analyzed for strain-compensated InGaN–AlGaN QW structures with indium contents of 28%, 22%, and 15% for lasers (light-emitting diodes) emitting at 480 (500), 440 (450), and 405 nm (415 nm) spectral regimes, respectively. The spontaneous emission spectra show significant improvement of the radiative emission for strain-compensated QW for all three structures compared to the corresponding conventional InGaN QW, which indicates the enhanced radiative efficiency for light emitting diodes. Our studies show the improvement of the optical gain and reduction of the threshold current density from the use of strain-compensated InGaN–AlGaN QW as active regions for diode lasers.**

***Index Terms*—Diode lasers, gain media, InGaN QW, light-emitting diodes (LEDs), self-consistent optical gain, strain-compensated quantum-well (QW) lasers, threshold current density.**

I. Introduction

THE InGaN-based visible light emitting diodes and lasers have gained considerable attention due to prospective applications in medical diagnostics, optical storage, full color display, and solid state lighting. Conventional III–Nitride gain media emitting in the visible regime is mainly based on the type-I InGaN quantum well (QW) with GaN barriers [1]–[5]. One of the major challenges that prevent high performance InGaN–GaN QW is the large spontaneous and piezoelectric polarization in the QW, which induces the low electron and hole wave functions overlap ($\Gamma_{\mathrm{e\_hh}}$), especially for QW with high indium content and thick QW active layer. Recently, several approaches have been proposed to suppress the charge separation effect in InGaN QW active region, as follow 1) nonpolar InGaN QW growth [6]; 2) the use of δ-AlGaN layer in InGaN QW [7], [8]; 3) staggered InGaN QW [9], [10]; and 4) type-II InGaN–GaNAs QW [11].

Another important limitation for the conventional type-I InGaN QW structure is the high threading dislocation density in III–Nitrides induced by large lattice mismatch between InGaN and GaN. Recently, we have proposed the use of strain-compensated InGaN–AlGaN QW structure employing thin (~1-nm) tensile-strained AlGaN barriers to surround the compressively strained InGaN QW [12], [13]. The use of strain-compensated InGaN–AlGaN QW was proposed previously [12], and the analysis taking into account of the carrier screening was presented in [13].

In this work, we present a comprehensive analysis of spontaneous emission, gain properties, and threshold current densities for strain-compensated $In_xGa_{1-x}N$–$Al_yGa_{1-y}N$ QW structures emitting in the 400–500 nm spectral regimes. The spontaneous emission, optical gain properties, and threshold current densities of the strain-compensated $In_xGa_{1-x}N$–$Al_yGa_{1-y}N$ QW were compared with those of the conventional (uncompensated) $In_xGa_{1-x}N$–GaN QW. The analysis took into account energy dispersion by using the 6-band $\boldsymbol{k} \cdot \boldsymbol{p}$ model, taking into account the strain, polarization fields, and carrier screening. The detailed theoretical and numerical model to analyze the self-consistent model are also presented and discussed. The studies focused on 1) the optimization of the strain-compensated QW lasers and LEDs emitting in the green spectral regime by using $In_{0.28}Ga_{0.72}N$–$Al_{0.2}Ga_{0.8}N$ QW active region, and 2) comparison studies of $In_xGa_{1-x}N$–$Al_yGa_{1-y}N$ QW with various In-contents for active regions emitting in the ultraviolet, blue, and green regimes. The compositions of the In-contents studied here range from 15%, 22%, up to 28%, corresponding to active regions emitting in the wavelengths of 405 (415), 440 (450), and 480 nm (500 nm) for lasers (light emitting diodes) applications.

The use of tensile barriers to surround compressively strained QW leads to a strain-compensated structure, which leads to a reduction in the strain energy and strain-misfit dislocation density inside the compressively strained QW. Similar concept of strain-compensated QW had also been previously applied for InGaAsN QW and InGaAs QW active regions by employing tensile GaAsP barriers, resulting in high-performance 1200–1400 nm emitting diode lasers on GaAs substrate [14]–[16]. The use of tensile AlGaN barriers surrounding the

Manuscript received April 07, 2008; revised May 21, 2008. This work was supported in part by the National Science Foundation (NSF)-ECCS Award #0701421, in part by the Department of Defense-Army Research Laboratory, in part by US Department of Energy-NETL, and in part by Peter C. Rossin Assistant Professorship.

The authors are with the Center for Optical Technologies, Department of Electrical and Computer Engineering, Lehigh University, Bethlehem, PA 18015 USA (e-mail: hoz207@lehigh.edu; raa4@lehigh.edu; ee@lehigh.edu; Tansu@Lehigh.Edu).

Color versions of one or more of the figures in this paper are available online at http://ieeexplore.ieee.org.

Digital Object Identifier 10.1109/JQE.2008.2004000

compressively strained InGaN QW leads to strain-compensated InGaN–AlGaN QW active regions. By reducing the strain-misfit dislocation density in the strain-compensated QW, the defect nonradiative recombination process will be suppressed leading to a reduction of nonradiative recombination current density in QW.

On the other hand, the use of larger bandgap barriers of AlGaN also leads to improved carrier confinement in the InGaN QW [17], which is important for achieving high performance LEDs and lasers operating at high temperature [18]–[20]. The use of InGaN–AlGaN QW has resulted in improvements in photoluminescence and radiative efficiency of 400-nm emitting LEDs by ~2-times [17]. The improvements were mainly attributed to the improved carrier confinement in the QW [17]. In addition to the improved carrier confinement in QW [17], however, our finding (Section VI) indicates that the improvement in the radiative efficiency of the strain-compensated QW LEDs can also be attributed to its improved spontaneous emission radiative recombination rate $(R_{\rm sp})$ by 50–80% for carrier densities (n) in the range of $2-10\times10^{18}$ cm^{-3}. In this work, we specifically address the spontaneous emission characteristics and optical gain properties of the strain-compensated InGaN–AlGaN QW active regions, and its feasibility for implementation in laser diodes.

The concept of strain-compensated InGaN–AlGaN QW will be introduced in Section II. The theoretical and numerical formulation of the analysis including the self-consistent model will be presented in Section III, followed by the details of the band and material parameters in Section IV. The momentum matrix elements characteristics for both QW structures will be discussed in Section V. The spontaneous emission and optical gain results will be discussed in Sections VI and VII, respectively. The threshold analysis and feasibility of the strain-compensated InGaN–AlGaN QW as laser active regions will be discussed in Section VIII. In Section IX, the comparison of the spontaneous emission and gain properties with different indium (In) contents will be discussed.

II. Strain-Compensated InGaN–AlGaN QW

Fig. 1 shows schematics of strain-compensated $In_xGa_{1-x}N$–$Al_yGa_{1-y}N$ QW structure. The lattice constant of $In_xGa_{1-x}N$ is larger than that of the GaN, which induce the compressive strain in the QW. By utilizing the $Al_yGa_{1-y}N$ barrier, which has smaller lattice constant than GaN, the tensile strain in the AlGaN layers help to compensate the compressive strain in the QW. This paper will analyze the following three structures: 24-Å $In_{0.15}Ga_{0.85}N$ QW $(\Delta a/a \sim +1.68\%)$, 24-Å $In_{0.22}Ga_{0.78}N$ QW $(\Delta a/a \sim +2.46\%)$, and 24-Å $In_{0.28}Ga_{0.72}N$ QW $(\Delta a/a \sim +3.13\%)$. In the corresponding strain-compensated QW structures, we employ thin 1-nm $Al_{0.2}Ga_{0.8}N$ barriers $(\Delta a/a \sim -0.47\%)$ surrounding the InGaN QW. The tensile AlGaN barriers lead to the improvement of the material quality, as well as the enhancement of the electron–hole wave functions overlap (Γ_{e_hh}). In addition to improved radiative recombination rate and gain from the enhanced overlap Γ_{e_hh}, the larger conduction (ΔE_c) and valence (ΔE_v) band offsets provided by the tensile AlGaN barrier layers lead to suppression of carrier leakage from the QW active region in particular for high temperature operation.

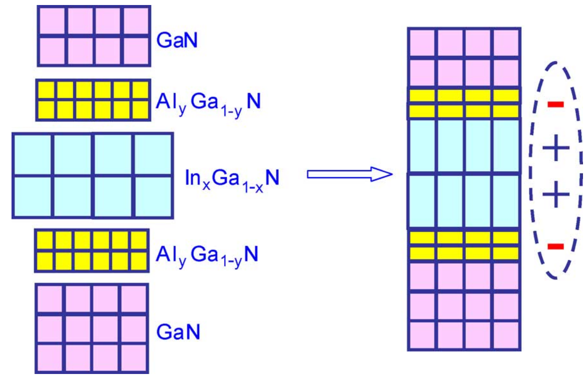

Fig. 1. Schematics of strain-compensated InGaN–AlGaN QW structure with compressively strained InGaN QW and tensile AlGaN barriers.

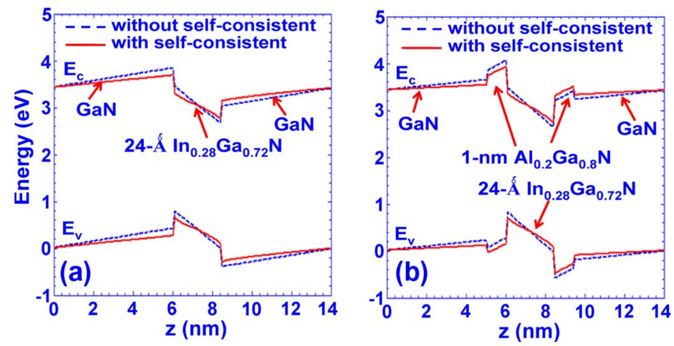

Fig. 2. Self-consistent band lineups of (a) conventional 24-Å $In_{0.28}Ga_{0.72}N$–GaN QW and (b) strain-compensated 24-Å $In_{0.28}Ga_{0.72}N$–$Al_{0.2}Ga_{0.8}N$ QW for carrier density $(n)=6\times10^{19}$ cm^{-3}.

Fig. 2 shows the energy band diagrams for the conventional 24-Å $In_{0.28}Ga_{0.72}N$ QW and strain-compensated 24-Å $In_{0.28}Ga_{0.72}N$–$Al_{0.2}Ga_{0.8}N$ QW active region with carrier density (n) calculated at $n = 6\times10^{19}$ cm^{-3}. As shown in Fig. 2, the band lineups (solid line) for both conventional and strain-compensated structures were calculated by taking into account the carrier screening effect. Our study shows that the carrier screening effect should be taken into account especially for carrier density at $n = 2\times10^{19}$ cm^{-3} and higher, which is important primarily for diode laser operation. The band lineups are flattened due to the carrier screening effect in the QW, which will induce the blue shift of the emission wave length and enhance the electron–hole wave functions overlap. For low carrier density $(n < 1\times10^{19}$ cm$^{-3})$ in LED devices, the carrier screening effect is less prominent and can typically be neglected in particular for $n < 5\times10^{18}$ cm^{-3}.

The spontaneous emission and optical gain properties were calculated by considering the energy band dispersion of the wurtzite semiconductor under a 6-band $\boldsymbol{k}\cdot\boldsymbol{p}$ formalism [21], [22]. The studies indicate the spontaneous emission and material gain are enhanced for the strain-compensated InGaN–AlGaN QW, resulting in a reduction in its threshold current density.

III. Theoretical and Numerical Formalisms

The calculation of the electron and hole wave functions is based on a 6-band $\boldsymbol{k}\cdot\boldsymbol{p}$ formalism for the band structure of wurtzite semiconductors [21], [22]. The numerical model takes into account the valence band mixing, strain effect, spontaneous and piezoelectric polarization, as well as the carrier screening effect. Because of the large bandgap of the III–Nitride materials, the coupling between the conduction and valence bands is neglected. In our current model, many-body Coulomb effects [23] and inhomogeneous broadening of In-content [4] in the QW are not taken into account. The theory discussion here follows the treatment developed in [13] and [22], and the theory development is presented for completeness. The electron energy bands are assumed to be parabolic. The hole energy bands are computed via 6 × 6 diagonalized $\boldsymbol{k}\cdot\boldsymbol{p}$ Hamiltonian matrix [21], [22], as follows:

$$H^{v}_{6\times6}(k)=\begin{bmatrix} H^{U}_{3\times3}(k) & 0 \\ 0 & H^{L}_{3\times3}(k)\end{bmatrix} \tag{1}$$

where $H^{U}_{3\times3}$ and $H^{L}_{3\times3}$ are 3 × 3 matrices defined as

$$H^{U}=\begin{bmatrix} F & K_t & -iH_t \\ K_t & G & \Delta-iH_t \\ iH_t & \Delta+iH_t & \lambda \end{bmatrix} \tag{2}$$

$$H^{L}=\begin{bmatrix} F & K_t & iH_t \\ K_t & G & \Delta+iH_t \\ -iH_t & \Delta-iH_t & \lambda \end{bmatrix}. \tag{3}$$

The matrix elements contain the general expressions for a strained wurtzite semiconductor are shown as follows:

$$F=\Delta_1+\Delta_2+\lambda+\theta,\quad G=\Delta_1-\Delta_2+\lambda+\theta \tag{4}$$

$$\lambda=\frac{\hbar^2}{2m_0}\left(A_1k_z^2+A_2k_t^2\right)+D_1\varepsilon_{zz}+D_2(\varepsilon_{zz}+\varepsilon_{yy}) \tag{5}$$

$$\theta=\frac{\hbar^2}{2m_0}\left(A_3k_z^2+A_4k_t^2\right)+D_3\varepsilon_{zz}+D_4(\varepsilon_{zz}+\varepsilon_{yy}) \tag{6}$$

$$K_t=\frac{\hbar^2}{2m_0}A_5k_t^2,\quad H_t=\frac{\hbar^2}{2m_0}A_6k_tk_z,\quad \Delta=\sqrt{2}\Delta_3 \tag{7}$$

where the strain parameters are related to lattice constant mismatch of the QW and barrier layers as follows:

$$\varepsilon_{xx}=\varepsilon_{yy}=\frac{a_0-a}{a} \tag{8}$$

$$\varepsilon_{zz}=-\frac{2C_{13}}{C_{33}}\varepsilon_{xx} \tag{9}$$

$$\varepsilon_{xy}=\varepsilon_{yz}=\varepsilon_{zx}=0 \tag{10}$$

with a_0 and a as the lattice constants of the GaN barriers and InGaN well layer, respectively. C_{13} and C_{33} are the stiffness constants of the InGaN well layer.

The magnitude of the in-plane wave vector in the k_x-k_y plane can be expressed as $k_t=\sqrt{k_x^2+k_y^2}$. Note that the parameter Δ_1 is the crystal-filed split energy, and the parameters Δ_2 and Δ_3 account for the spin-orbit interaction. The $A_i's$ are the effective mass parameters, and the $D_i's$ are the deformation potentials. These parameters are listed in Table I for the case of relevant binary alloys (GaN, InN, and AlN).

TABLE I
Material Parameters for GaN, AlN, and InN. The Values are Taken From [29] and [30]

Parameters	GaN	AlN	InN
Lattice constant (Å)			
a	3.189	3.112	3.545
c	5.185	4.982	5.703
Energy Parameters			
E_g (eV) at 300 K	3.437	6.00	0.6405
$\Delta_1(=\Delta_{cr})$ (eV)	0.010	-0.227	0.024
$\Delta_1=\Delta_2=\Delta_{so}/3$ (eV)	0.00567	0.012	0.00167
Conduction-band effective masses			
$m_{//}^*/m_0$ at 300K	0.21	0.32	0.07
$m_\perp^*/m_0$ at 300K	0.20	0.30	0.07
Valence-band effective mass parameters			
A_1	-7.21	-3.86	-8.21
A_2	-0.44	-0.25	-0.68
A_3	6.68	.58	7.57
A_4	-3.46	-1.32	-5.23
A_5	-3.40	-1.47	-5.11
A_6	-4.90	-1.64	-5.96
Deformation potentials (eV)			
a_{cz} (eV)	-7.1	-3.4	-4.2
a_{ct} (eV)	-9.9	-11.8	-4.2
D_1 (eV)	-3.6	-2.9	-3.6
D_2 (eV)	1.7	4.9	1.7
D_3 (eV)	5.2	9.4	5.2
D_4 (eV)	-2.7	-4.0	-2.7
Elastic stiffness constants			
C_{11} (GPa)	390	396	223
C_{12} (GPa)	145	137	115
C_{13} (GPa)	106	108	92
C_{33} (GPa)	398	373	224
Piezoelectric coefficients			
d_{13} (pmV^{-1})	-1.0	-2.1	-3.5
d_{33} (pmV^{-1})	1.9	5.4	7.6
Spontaneous Polarization			
P_{sp} (C/m^2)	-0.034	-0.090	-0.042

The numerical model also takes into account the electric field resulting from the spontaneous (P_{SP}) and piezoelectric (P_{PZ}) polarization fields. The spontaneous polarization uses the linear interpolation [24], and the piezoelectric polarization can be expressed as follows [25]:

$$P_{\mathrm{PZ}}=2d_{31}\left(C_{11}+C_{12}-\frac{2C_{13}^2}{C_{33}}\right)\varepsilon_{xx} \tag{11}$$

where d_{31} and C's are piezoelectric coefficient and elastic stiffness coefficients, respectively.

The existence of both built-in polarization fields in wurtzite III–Nitride semiconductors leads to energy band bending. The electrostatic fields in each layer $(j\text{th})$ as a result of total polarization fields can be expressed as [24]

$$E_j=\frac{\sum_k l_kP_k/\varepsilon_k-P_j\sum_k l_k/\varepsilon_k}{\varepsilon_j\sum_k l_k/\varepsilon_k} \tag{12}$$

where P is the total macroscopic polarization, ε is the static dielectric constant, and l is the thickness of each layers $(k\text{th}, j\text{th})$. The subscripts k and j correspond to the kth and jth layers. To ensure zero average electric field in the layers, note that the electric field expression in (12) needs to satisfy the periodic boundary conditions as follows [24]:

$$\sum_k l_k E_k = 0 \tag{13}$$

where the summation (k) consists of all layers including the QW active regions and barrier regions.

By using the calculated envelop functions, the optical transition matrix element relating nth-state in conduction band and mth-state in valence band can be computed by the following relations:

- TE-polarization ($\hat{x}$ or $\hat{y}$ polarization)

$$\begin{aligned}|(M_x)^\sigma_{nm}(k_t)|^2 \\ &= \frac{|\langle S|p_x|X\rangle|^2}{4}\cdot\left\{\left\langle \phi_n|g_m^{(1)}\right\rangle^2+\left\langle \phi_n|g_m^{(2)}\right\rangle^2\right\} \quad \text{for } \sigma=U \\ &= \frac{|\langle S|p_x|X\rangle|^2}{4}\cdot\left\{\left\langle \phi_n|g_m^{(4)}\right\rangle^2+\left\langle \phi_n|g_m^{(5)}\right\rangle^2\right\} \quad \text{for } \sigma=L.\end{aligned} \tag{14}$$

- TM-polarization ($\hat{z}$ polarization)

$$\begin{aligned}|(M_z)^\sigma_{nm}(k_t)|^2 &= \frac{|\langle S|p_z|Z\rangle|^2}{4}\cdot\left\langle \phi_n|g_m^{(3)}\right\rangle^2 \quad \text{for } \sigma=U \\ &= \frac{|\langle S|p_z|Z\rangle|^2}{4}\cdot\left\langle \phi_n|g_m^{(6)}\right\rangle^2 \quad \text{for } \sigma=L\end{aligned} \tag{15}$$

where ϕ_n and g_m are conduction and valence band confined states, respectively. The upper and lower Hamiltonian blocks are indicated by $\sigma = U$ and $\sigma = L$, respectively. In our calculations here, the linewidth broadening time (τ_s) is assumed to have Lorentzian shape with $\tau_S = 0.1$ ps. The details of the material parameters utilized in the calculation are listed in Table I.

Based on the Fermi's Goden rule, the spontaneous emission rate for TE $(e = x)$ or TM $(e = z)$ polarizations can be obtained by taking into account all interband transitions between nth conduction subbands and mth valence subbands as follows:

$$\begin{aligned}g^e_{\rm sp}(\hbar\omega) = \frac{2q^2\pi}{n_r c\varepsilon_0 m_0^2 \omega L_\omega}\sum_{\sigma=U,L}\sum_{n,m}\int\frac{k_t dk_t}{2\pi}|(M_e)^\sigma_{nm}(k_t)|^2 \\ \cdot\frac{f_n^c(k_t)\left(1-f^v_{\sigma m}(k_t)\right)(\gamma/\pi)}{\left(E^{cv}_{\sigma,nm}(k_t)-\hbar\omega\right)^2+\gamma^2}.\end{aligned} \tag{16}$$

The optical gains for the TE $(g^{\rm TE})$ and TM $(g^{\rm TM})$ polarizations are related to the spontaneous emission rate, as follows:

$$g^{\rm TE}(\hbar\omega)=g^x_{\rm sp}(\hbar\omega)\left[1-\exp\left(\frac{\hbar\omega-\Delta F}{k_B T}\right)\right] \tag{17a}$$

$$g^{\rm TM}(\hbar\omega)=g^z_{\rm sp}(\hbar\omega)\left[1-\exp\left(\frac{\hbar\omega-\Delta F}{k_B T}\right)\right]. \tag{17b}$$

Our analysis indicates that the TM-polarized optical gain $(g^{\rm TM})$ is negligible for the case of compressively strained InGaN QW, similar to the finding in [22]. Thus, the optical gain of the compressively strained InGaN QW systems is found as dominantly TE-polarized.

Note that the parameter ΔF is the separation of the quasi-Fermi levels of electrons (F_c) and holes (F_v). The parameter ΔF can be expressed as $\Delta F = F_c - F_v$, which depends on the injection carrier densities (n and p) shown as follows:

$$n = \frac{2}{L_w}\sum_n\int\frac{k_t dk_t}{2\pi}f_n^c(k_t) \tag{18}$$

$$p = \frac{1}{L_w}\sum_{\sigma=U,L}\sum_m\int\frac{k_t dk_t}{2\pi}\left(1-f^v_{\sigma m}(k_t)\right). \tag{19}$$

Note that the $f_n^c(k_t)$ and $f^v_{\sigma m}(k_t)$ are the Fermi–Dirac distribution functions for the electrons in conduction band and valence band, given as follows:

$$f_n^c(k_t) = \frac{1}{1+\exp\left(\frac{E_n^c(k_t)-F_c}{k_B T}\right)} \tag{20}$$

$$f^v_{\sigma m}(k_t) = \frac{1}{1+\exp\left(\frac{E^v_{\sigma,m}(k_t)-F_v}{k_B T}\right)}. \tag{21}$$

For the calculation of the spontaneous emission rate, we took into account both the TE and TM polarizations. The total momentum matrix element is the average of two TE-polarization components and one TM-polarization component [22], which can be expressed as follows:

$$|M_{\rm sp}|^2 = \frac{1}{3}\left(2|M_x|^2+|M_z|^2\right). \tag{22}$$

The total spontaneous emission rate per unit volume per unit energy interval $(s^{-1}\ \mathrm{cm}^{-3}\ \mathrm{eV}^{-1})$ can be written as follows:

$$r^{\rm spon}(E=\hbar\omega) = \frac{n_e^2 w^2}{\pi^2\hbar c^2}\frac{2\left(2g^x_{\rm sp}+g^z_{\rm sp}\right)}{3}. \tag{23}$$

The total spontaneous emission rate per unit volume $(s^{-1}\ \mathrm{cm}^{-3})$ is obtained by integrating the (23) over the entire frequency range as follow [27]

$$R_{\rm sp} = \int_0^\infty r^{\rm spon}(\hbar\omega)d(\hbar\omega). \tag{24}$$

Thus, the radiative recombination current density $(\mathrm{A/cm}^2)$ is defined as [27]

$$J_{\rm rad} = qdR_{\rm sp}. \tag{25}$$

In the calculations of the spontaneous emission spectra and optical gain for polar semiconductors (i.e., InGaN QW), it is important to include all possible transitions between electron and hole confined states in the QW. As the polarization field-induced band bending in the III–Nitride QW leads to the breaking of the orthogonality condition between states with different quantum numbers, e.g., $E_1^c - E_2^{hh}$, $E_2^c - E_1^{hh}$, and so on; transitions between such states—which are traditionally 'forbidden' in nonpolar semiconductors—may have an appreciable transition probabilities as indicated by the nonzero values of their matrix elements, and therefore have to be included in the calculation [26].

The calculations of the eigen energies and wave functions in our analysis here are based on a self-consistent model by solving the Poisson equation [27] expressed as follows:

$$\frac{\partial}{\partial z}\left(\varepsilon \frac{\partial V_{sc}}{\partial z}\right) = -\rho(z) \tag{26}$$

where the term V_{sc} incorporates the potential function including the effect of the spontaneous and piezoelectric polarizations, and $\rho(z)$ is the charge distribution given by

$$\rho(z) = |e|\left[p(z) - n(z)\right]. \tag{27}$$

Note that the electron and hole concentrations are related to the wave functions of the nth conduction subband $[\phi_n(z)]$ and the mth valence subband $[g_m(z)]$ as well as their corresponding surface electron concentration (N_n) and surface hole concentration (P_m) as follows:

$$n(z) = \sum_n |\phi_n(z)|^2 N_n \tag{28}$$

$$p(z) = \sum_m |g_m(z)|^2 P_m. \tag{29}$$

The surface electron concentration in the nth conduction band can be expressed as

$$N_n = 2\int_0^\infty \frac{2\pi k_t}{(2\pi)^2}\frac{1}{1+e^{[E_{en}(k_t)-F_c]/k_BT}}dk_t \tag{30}$$

and the surface hole concentration in the mth valence band is given by

$$P_m = 2\int_0^\infty \frac{2\pi k_t}{(2\pi)^2}\frac{1}{1+e^{[F_v-E_{hm}(k_t)]/k_BT}}dk_t. \tag{31}$$

The inclusion of self-consistent electrostatic potential $V_{sc}(z)$ will modify both the total potential profiles for electrons $[U_e(z)]$ and holes $[U_h(z)]$ as follows:

$$U_e(z) = U_0^e(z) - |e|V_{sc}(z) \tag{32}$$

$$U_h(z) = U_0^h(z) - |e|V_{sc}(z). \tag{33}$$

Thus, the self-consistent Schrödinger equations taking into account the carrier screening effect for electrons and holes can be expressed as follows:

$$\left[-\frac{\hbar^2}{2m_e^*}\frac{d^2}{dz^2} + U_e(z)\right]\phi(z) = E_e\phi(z) \tag{34}$$

$$\left[\frac{\hbar^2}{2m_h^*}\frac{d^2}{dz^2} + U_h(z)\right]g(z) = E_h g(z). \tag{35}$$

The numerical flow chart to compute the spontaneous emission and optical gain of III–Nitride semiconductor nanostructure is shown in Fig. 3. Based on the general formalism for the calculation of the band structure for semiconductor heterostructure/nanostructure (i.e., quantum well or quantum dots systems), finite difference method is used to solve the Schrödinger equations similar to the treatment in [28]. The spatial interval for the finite difference method is 1 Å. The band-edge potential has to be solved self-consistently due to the interdependent of the carrier distribution and band-edge potential. Therefore, a closed loop is formed to solve the Schrödinger equations and Poisson equation alternately until the eigen energy converges. Then the wave functions are simultaneously solutions for both Schrödinger and Poisson equations. In the self-consistent calculation, the convergence condition is set such as the error of the eigen energy converge to less than 0.1%, which requires 15 up to 20 iterations for each carrier density computation.

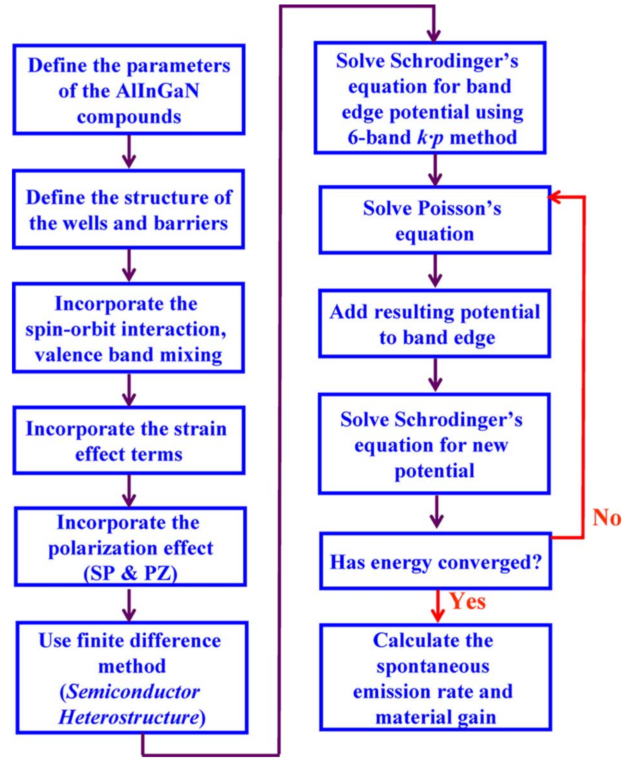

Fig. 3. Numerical flow chart of the simulation process for self-consistent model of 6-band $\boldsymbol{k}\cdot\boldsymbol{p}$ for wurtzite semiconductor QW active region.

IV. Band Structure and Parameters

The in-plane valence band dispersions of both the conventional InGaN–GaN QW and strain-compensated InGaN–AlGaN QW structures were calculated from (1)–(13) using the parameters of GaN, InN, and AlN shown in Table I [29], [30]. The bowing parameters to calculate the bandgap for InGaN and AlGaN are 1.4 eV and 0.8 eV, respectively. Other parameters for the ternary alloys (AlGaN, InGaN) use linear interpolation of the binary alloy (InN, GaN, AlN) parameters.

Fig. 4 shows the band-edge valence band structures for the conventional and strain-compensated structures, which were calculated self-consistently at the carrier density level $n = 6 \times 10^{19}$ cm^{-3}. First, for both the conventional and strain-compensated QW structures, the HH and LH bands near the band edges have very similar effective masses. While far away from the zone center, the HH band has a heavier effective mass than that of the LH band. By comparing Fig. 4(a) and 4(b), the heavy hole and light hole subband energies will be very

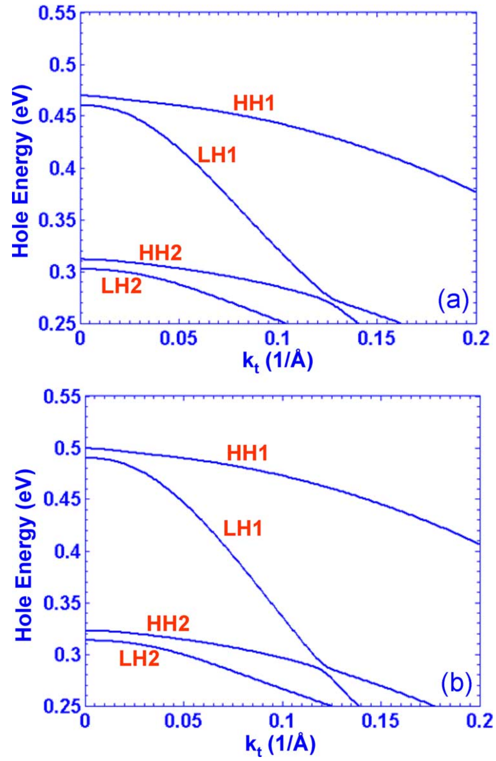

Fig. 4. Valence band structure for the (a) conventional 24-Å $In_{0.28}Ga_{0.72}N$–GaN QW and (b) strain-compensated 24-Å $In_{0.28}Ga_{0.72}N$–$Al_{0.2}Ga_{0.8}N$ QW with free-carrier screening. The carrier density is 6×10^{19} cm^{-3}.

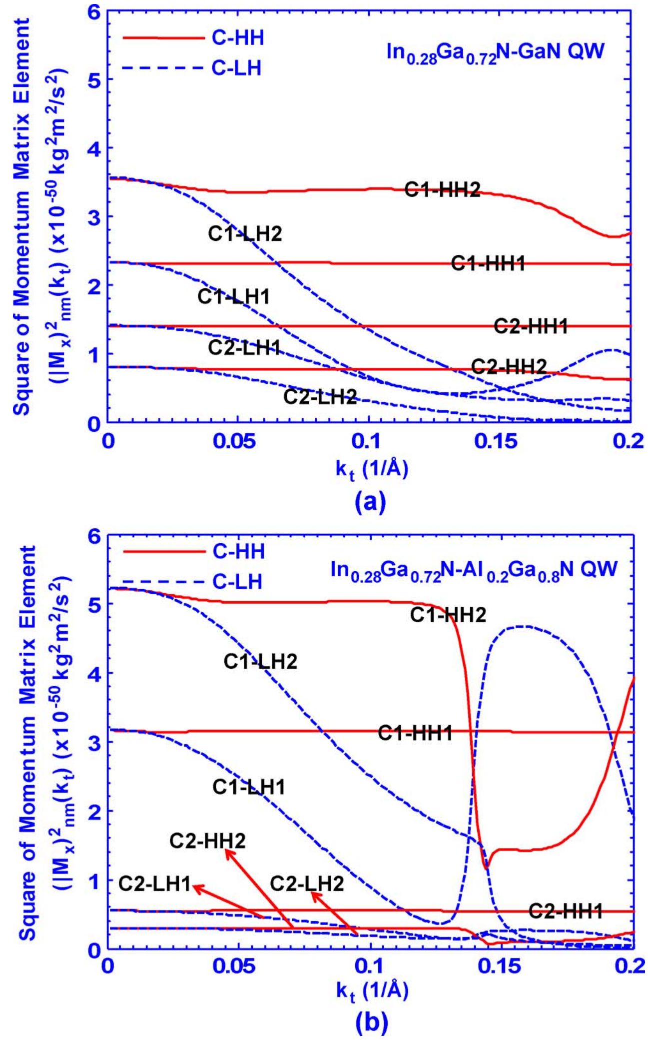

Fig. 5. Square of momentum matrix elements as a function of the in-plane wave vector k_t in the TE-polarization for (a) conventional 24-Å $In_{0.28}Ga_{0.72}N$–GaN QW and (b) strain-compensated 24-Å $In_{0.28}Ga_{0.72}N$–$Al_{0.2}Ga_{0.8}N$ QW. The carrier density is 3×10^{19} cm^{-3}.

close for both InGaN QW structures. The density of states of the heavy hole subbands will be much larger than that of the light hole subbands, in particular for the strain-compensated QW structure. Second, the HH1 and LH1 subbands shift up in the strain-compensated structure, and the energy separation between $n = 1$ and $n = 2$ is larger compared to the conventional structure.

V. Momentum Matrix Elements Characteristics

The (14) and (15) describe the momentum matrix elements for TE polarization and TM polarization, respectively. Fig. 5(a) and 5(b) show the dispersion relation of the square of the momentum matrix elements $(M_x)^2_{\rm nm}(k_t)$ for TE-polarization as a function of the in-plane wave vector k_t for conventional $In_{0.28}Ga_{0.72}N$–GaN QW [Fig. 5(a)] and strain-compensated $In_{0.28}Ga_{0.72}N$–$Al_{0.2}Ga_{0.8}N$ QW (Fig. 5(b)) with transitions between C1-HH1, C1-LH1, C1-HH2, C1-LH2, C2-HH1, C2-LH1, C2-HH2, and C2-LH2 at carrier density of $n = 3 \times 10^{19}$ cm^{-3}.

By comparing the transition matrix elements among all the confined state transitions, the C1-HH1, C1-LH1, C1-HH2, and C1-LH2 transitions are comparatively strong, which contribute dominantly to the spontaneous emission rate. The C2-HH1, C2-LH1, C2-HH2, and C2-LH2 transition matrix elements for both structures are comparatively weaker. Note that the strain-compensated structure shows stronger transitions for the C1-HH1, C1-LH1, C1-HH2 and C1-LH2 as compared to those of the conventional InGaN–GaN QW structure.

Fig. 6(a) and 6(b) show the relation of $(\mathrm{M}_x)^2_{\rm nm}(k_t)$ at $k_t = 0$ as a function of the carrier density. Note that the transition matrix element at the zone center $(k_t = 0)$ between the conduction band and heavy-hole subband is similar to that between the conduction band and light-hole subband. From the comparison, as the carrier density is increasing, the $(M_x)^2_{\rm nm}(k_t = 0)$ increase for C1-HH1, C1-LH1, C1-HH2, C1-LH2, C2-HH1 and C2-LH1 transitions. However, the C2-HH2 and C2-LH2 matrix elements decrease, as the carrier density increases. Note that the dominant terms of the matrix element square at zone center $(k_t = 0)$ of the strain compensated InGaN–AlGaN QW (C1-HH1, C1-LH1, C1-HH2 and C1-LH2), which contribute to

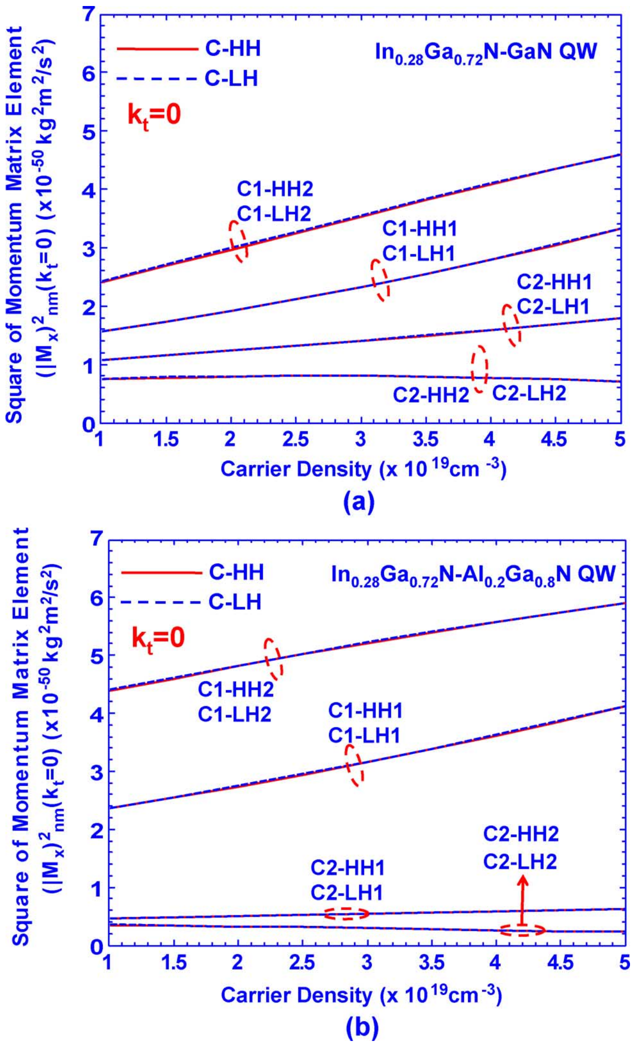

Fig. 6. Square of momentum matrix elements at zone center ($k_t = 0$) using the self-consistent model as a function of the carrier density for (a) conventional 24-Å $In_{0.28}Ga_{0.72}N$–GaN QW and (b) strain-compensated 24-Å $In_{0.28}Ga_{0.72}N$–$Al_{0.2}Ga_{0.8}N$ QW.

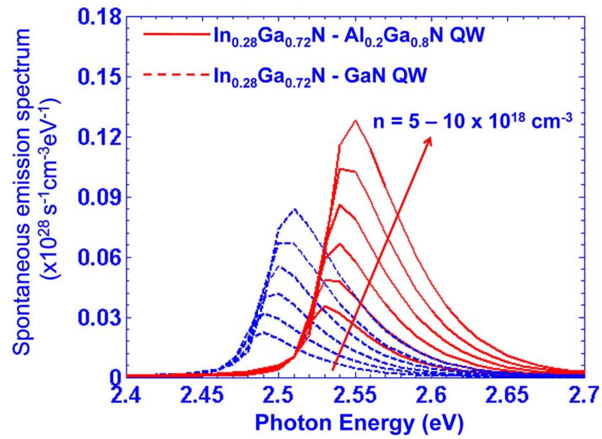

Fig. 7. Spontaneous emission spectra of 24-Å conventional $In_{0.28}Ga_{0.72}N$ QW and strain-compensated 24-Å $In_{0.28}Ga_{0.72}N$–$Al_{0.2}Ga_{0.8}N$ QW for $n = 5 \times 10^{18}$ cm^{-3} up to 10×10^{18} cm^{-3}.

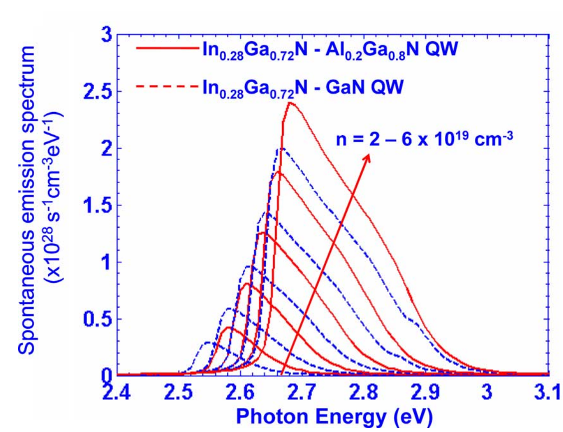

Fig. 8. Spontaneous emission spectra of 24-Å conventional $In_{0.28}Ga_{0.72}N$ QW and strain-compensated 24-Å $In_{0.28}Ga_{0.72}N$–$Al_{0.2}Ga_{0.8}N$ QW for $n = 2 \times 10^{19}$ cm^{-3} up to 6×10^{19} cm^{-3}.

the spontaneous emission rate, are larger than those of the conventional InGaN QW structure.

VI. Spontaneous Emission Characteristics

Following (16) and (23), the spontaneous emission spectra for both conventional $In_{0.28}Ga_{0.72}N$–GaN QW and strain-compensated $In_{0.28}Ga_{0.72}N$–$Al_{0.2}Ga_{0.8}N$ QW were calculated from low carrier density ($n = 2 \times 10^{18}$ cm^{-3}) up to high carrier density ($n = 6 \times 10^{19}$ cm^{-3}) at $T = 300$ K, as shown in Fig. 7 and Fig. 8. Note that the carrier densities (n) refer to the densities of the injected carrier that recombines radiatively in the QW active region. For the low carrier density regime ranging from $n = 5 \times 10^{18}$ cm^{-3} up to $n = 10 \times 10^{18}$ cm^{-3} (Fig. 7), the peaks of the spontaneous emission spectra for both conventional QW and strain-compensated QW exhibited slight blueshift, which can be attributed primarily from the state filling effect (for $n < 1 \times 10^{19}$ cm^{-3}). The spontaneous emission spectra for the strain-compensated QW structure are enhanced by 50–60% for low carrier density regime in comparison to those of the conventional structure.

In Fig. 8, the spontaneous emission spectra are compared for conventional and strain-compensated QW structures at high carrier density regime (from $n = 2 \times 10^{19}$ cm^{-3} up to $n = 6 \times 10^{19}$ cm^{-3}). In contrast to Fig. 7, the peaks of spontaneous emission spectra in Fig. 8 show large blue shifts for both conventional and strain-compensated QW structures for increasing carrier density, and these blueshifts can be attributed to the enhanced carrier screening effect for high carrier density operation. In the high carrier density regime, the peak spontaneous emission spectra of the strain-compensated InGaN–AlGaN QW structure are found to be approximately 20–50% higher than that of the conventional QW.

Figs. 9(a) and 9(b) illustrate the spontaneous emission radiative recombination rate per unit volume (R_{sp}) of strain-compensated 24-Å $In_{0.28}Ga_{0.72}N$–$Al_{0.2}Ga_{0.8}N$ QW and conventional 24-Å $In_{0.28}Ga_{0.72}N$–GaN QW plotted against carrier density (n), for the low carrier density ($n = 2 \times 10^{18}$ cm^{-3} up to 10×10^{18} cm^{-3}) and high carrier density ($n = 2 \times 10^{18}$ cm^{-3} up to 6×10^{19} cm^{-3}) regimes, respectively. The spontaneous emission radiative recombination rate per unit volume (R_{sp}) can be

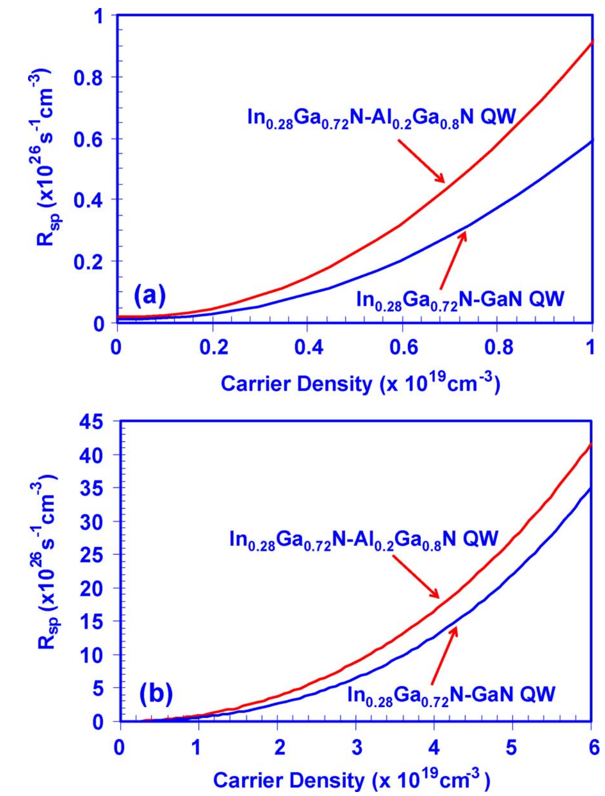

Fig. 9. Spontaneous emission radiative recombination rate per unit volume as a function of carrier density at 300 K for conventional 24-Å $In_{0.28}Ga_{0.72}N$–GaN QW and strain-compensated 24-Å $In_{0.28}Ga_{0.72}N$–$Al_{0.2}Ga_{0.8}N$ QW, calculated for a) low carrier density from $n = 2 \times 10^{18}$ cm^{-3} up to 1×10^{19} cm^{-3}, and b) high carrier density from $n = 2 \times 10^{18}$ cm^{-3} up to 6×10^{19} cm^{-3}.

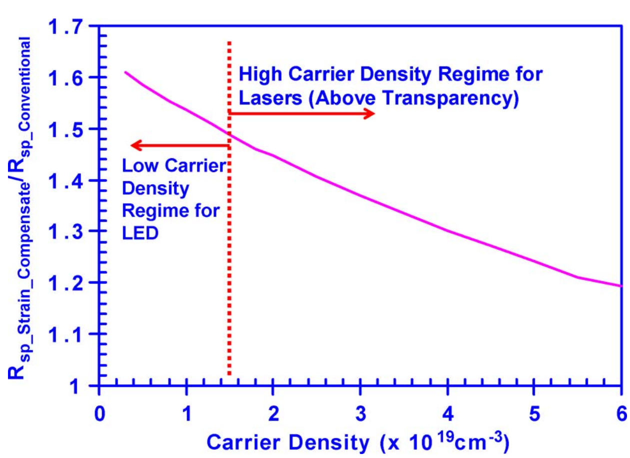

Fig. 10. Ratio of spontaneous emission radiative recombination rate (R_{sp}) for strain-compensated 24-Å $In_{0.28}Ga_{0.72}N$–$Al_{0.2}Ga_{0.8}N$ QW and conventional 24-Å $In_{0.28}Ga_{0.72}N$–GaN QW as function of carrier density at temperature of 300 K. The ratio is plotted from carrier density $n = 2 \times 10^{18}$ cm^{-3} up to 6×10^{19} cm^{-3}.

obtained from (24). Fig. 10 shows the ratio of the spontaneous emission radiative recombination rate (Rsp) for strain-compensated 24-Å $In_{0.28}Ga_{0.72}N$–$Al_{0.2}Ga_{0.8}N$ QW and conventional 24-Å $In_{0.28}Ga_{0.72}N$–GaN QW as function of carrier density at temperature of 300 K, for carrier density $n = 2 \times 10^{18}$ cm^{-3} up to $n = 6 \times 10^{19}$ cm^{-3}.

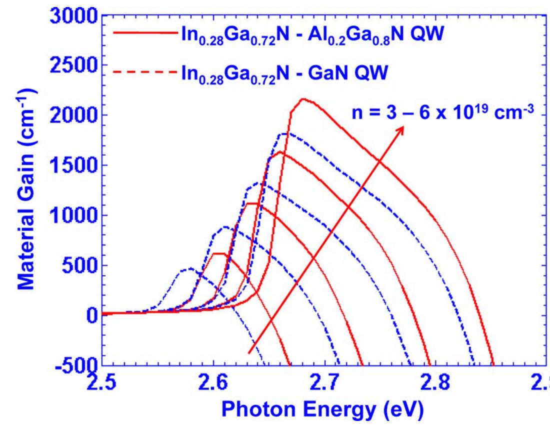

Fig. 11. TE-polarized optical gain spectra of strain-compensated 24-Å $In_{0.28}Ga_{0.72}N$–$Al_{0.2}Ga_{0.8}N$ QW and conventional 24-Å $In_{0.28}Ga_{0.72}N$–GaN QW for carrier density (n) from 3×10^{19} cm^{-3} up to 6×10^{19} cm^{-3}.

The typical carrier density for LED operation ranges from $2 - 5 \times 10^{18}$ cm^{-3} up to 1×10^{19} cm^{-3} [31]–[33]. As shown in Figs. 9(a) and 10, the strain-compensated QW exhibited 50–60% enhancement of the radiative recombination rate for the low carrier density regime of $n = 2 \times 10^{18}$ cm^{-3} up to $n = 10 \times 10^{18}$ cm^{-3}. Thus, the significant enhancement of the spontaneous emission radiative recombination rate for the strain-compensated QW will lead to a significant improvement in the radiative efficiency of the LEDs.

For laser operation, the typical threshold carrier density of InGaN QW lasers ranges from 3.5×10^{19} cm^{-3} up to 7×10^{19} cm^{-3} [34]. As shown in Figs. 9(b) and 10, for the case of $n = 3 \times 10^{19}$ cm^{-3} ($n = 5 \times 10^{19}$ cm^{-3}), the strain-compensated InGaN QW structure exhibits approximately 37% (25%) higher spontaneous emission radiative recombination rate of $R_{sp} = 8.9 \times 10^{26}$ s^{-1} cm^{-3} ($R_{sp} = 2.73 \times 10^{27}$ s^{-1} cm^{-3}) than that of the conventional one of $R_{sp} = 6.5 \times 10^{26}$ s^{-1} cm^{-3} ($R_{sp} = 2.19 \times 10^{27}$ s^{-1} cm^{-3}). The improvement of the spontaneous emission rate by using the strain-compensated InGaN–AlGaN QW is due to the better carrier confinement of the AlGaN barriers, which induce the higher electron and hole wave function overlap. The enhancement of the spontaneous emission rate indicates that the strain-compensated structure can be applied for LEDs with higher radiative efficiency.

VII. Optical Gain Characteristics

By using the (16) and (17.a), the TE optical gain spectra were calculated self-consistently for both conventional and strain-compensated structures. Fig. 11 shows the comparison of gain spectra for both structures at carrier densities from 3×10^{18} cm^{-3} up to 6×10^{19} cm^{-3} at $T = 300$ K. The optical gain is enhanced by using the strain-compensated structure. As the increase of the carrier density, the peak of the gain spectra for both structures shift to the shorter wavelength due to the carrier screening effect.

Fig. 12 shows the peak optical gain for both conventional and strain-compensated structures. The transparency carrier densities (n_{tr}) for both conventional and strain-compensated QW structures are relatively similar in the range of $n_{tr} \sim 1.5 \times$

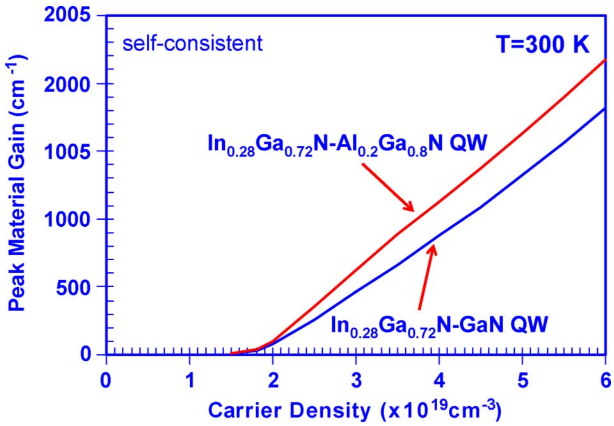

Fig. 12. Peak material gain as a function of carrier density at 300 K for conventional 24-Å $In_{0.28}Ga_{0.72}N$–GaN QW and strain-compensated 24-Å $In_{0.28}Ga_{0.72}N$–$Al_{0.2}Ga_{0.8}N$ QW.

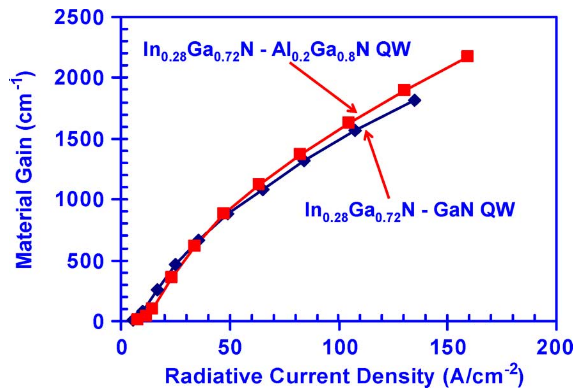

Fig. 13. Material gain versus radiative current density of strain-compensated 24-Å $In_{0.28}Ga_{0.72}N$–$Al_{0.2}Ga_{0.8}N$ QW and conventional 24-Å $In_{0.28}Ga_{0.72}N$–GaN.

10^{19} cm^{-3}. The strain-compensated QW structure exhibited increase in the peak optical gain for carrier density (n) above transparency, in comparison to that of conventional QW. For example in the relatively high carrier density regime $n = 5 \times 10^{19}$ cm^{-3} (near threshold condition), the peak optical gain of the strain-compensated 24-Å $In_{0.28}Ga_{0.72}N$–$Al_{0.2}Ga_{0.8}N$ QW structure exhibited peak material gain $(\mathrm{g_p})$ of 1629 cm^{-1}, which corresponds to improvement of 23.3% in comparison to that of conventional 24-Å $In_{0.28}Ga_{0.72}N$–GaN QW structure ($\mathrm{g_p}$ = 1321.7 cm^{-1}, for $n = 5 \times 10^{19}$ cm^{-3}).

The differential gain of strain-compensated QW is found to be optimum ($\mathrm{dg/dn} = 5.48 \times 10^{-17}$ cm^2) at carrier density $n = 3.0 \times 10^{19}$ cm^{-3}, which is approximately 29.2% higher than that of conventional QW ($\mathrm{dg/dn} = 4.24 \times 10^{-17}$ cm^2). For the case without considering screening effect, the maximum differential gain is found at near transparency condition. However, for the case taking into consideration the screening effect, the optimum differential gain exhibits low dg/dn at near transparency due to the 'softer' transparency condition. It is important to note here by using the strain-compensated structure, the optical gain and differential gain are improved compared to the conventional structure, which leads to the reduction of the nonradiative recombination current density (the detail will be discussed in Section VIII).

VIII. Radiative Current Density and Threshold Current Density Analysis

To study the feasibility of strain-compensated InGaN–AlGaN QW as active region for diode lasers application, we employed a laser structure with single QW as active region similar to the structure reported in [35]. The active region of 24-Å $In_{0.28}Ga_{0.72}N$–$Al_{0.2}Ga_{0.8}N$ QW is implemented as the active region of the laser structure for emission in the 480-nm regime. The optical confinement (Γ_{opt}) and internal loss (α_i) are 0.01 (1%) and 8.6 cm^{-1}, respectively. The laser cavity length is assumed as 650 μm with end facets reflectivities of 95% and 56%, which correspond to mirror loss α_{m} = 4.85 cm^{-1}. The threshold gain (g_{th}) required for lasing is estimated as $g_{\mathrm{th}} \sim 1345$ cm^{-1}. From the peak gain—carrier density relation in Fig. 12, the threshold carrier density (n_{th}) required to achieve threshold condition for the strain-compensated QW is $n_{\mathrm{th}} = 4.4 \times 10^{19}$ cm^{-3}, which corresponds to ~13.7% reduction compared to that ($n_{\mathrm{th}} = 5.1 \times 10^{19}$ cm^{-3}) of the conventional InGaN–GaN QW structure. It is important to note that the reduction in the threshold carrier density is important for minimizing the nonradiative recombination rate, which in turn will lead to reduction in the nonradiative component of the threshold current density.

The radiative recombination current density (J_{Rad}) for the QW can be obtained from (25). From the calculated material gain (Fig. 12) and radiative spontaneous emission rate [Fig. 9(b)], the relation of material gain (g_p) versus radiative current density (J_{Rad}) can be obtained as shown in Fig. 13. Note that the strain-compensated QW exhibited higher differential gain resulting in lower threshold carrier density (Fig. 12), however both conventional and strain-compensated QW exhibited relatively similar $\mathrm{g_p}$ versus $\mathrm{J_{Rad}}$ relation (as shown in Fig. 13). Thus, the key advantage of the implementation of the strain-compensated QW is the reduction in threshold carrier density, which leads to a reduction in the threshold current density. The total recombination mechanisms include both the radiative and nonradiative recombination processes. In our analysis, we only consider the monomolecular current density ($J_{\mathrm{mono}} = A \cdot n$) as the nonradiative term, where A is the monomolecular recombination constant. The Auger current density (J_{Auger}) component is neglected, as this recombination is negligible for wide bandgap InGaN QW [36].

The relationships of the peak material gain as a function of the total recombination current density ($\mathrm{J_{total} = J_{rad} + J_{nr}}$) for both the strain-compensated 24-Å $In_{0.28}Ga_{0.72}N$–$Al_{0.2}Ga_{0.8}N$ QW and conventional 24-Å $In_{0.28}Ga_{0.72}N$–GaN QW structures are shown in Fig. 14. The analysis consists of QW active regions with three different monomolecular recombination constants [26], $A = 6 \times 10^8$ s^{-1}, $A = 1 \times 10^9$ s^{-1} and $A = 1.5 \times 10^9$ s^{-1}. For laser structure employing single QW with threshold gain (g_{th}) of 1345 cm^{-1}, the calculated threshold current densities for the strain-compensated QW lasers are 1120 A/cm^2, 1800 A/cm^2 and 2650 A/cm^2 for the case of $A = 6 \times 10^8$ s^{-1}, $A = 1 \times 10^9$ s^{-1}, and $A = 1.5 \times 10^9$ s^{-1}, respectively. The comparisons of the threshold current densities for both strain-compensated InGaN–AlGaN QW and conventional

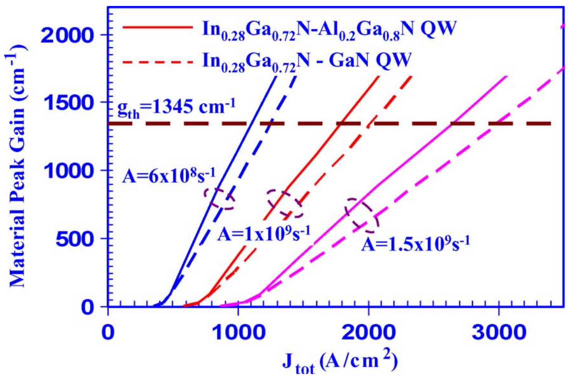

Fig. 14. Material gain versus radiative current density for conventional 24-Å $In_{0.28}Ga_{0.72}N$–GaN QW and strain-compensated 24-Å $In_{0.28}Ga_{0.72}N$–$Al_{0.2}Ga_{0.8}N$ QW.

TABLE II
THE TOTAL THRESHOLD CURRENT DENSITY (J_{th_total}) FOR 24-Å $In_{0.28}Ga_{0.72}N$–GaN QW AND STRAIN-COMPENSATED 24-Å $In_{0.28}Ga_{0.72}N$–$Al_{0.2}Ga_{0.8}N$ QW WITH VARIOUS MONOMOLECULAR RECOMBINATION RATES (A)

Monomolecular recombination rate	Total threshold current density (J_{th_total}) for strain compensated InGaN-AlGaN QW (A/cm^2)	Total threshold current density (J_{th_total}) for conventional InGaN-GaN QW (A/cm^2)
A=6x10^8 s^{-1}	1120	1260
A=1x10^9 s^{-1}	1800	2025
A=1.5x10^9 s^{-1}	2650	3020

InGaN–GaN QW lasers are shown in Table II, for various monomolecular recombination coefficients. Note that the reduction of the threshold current densities observed in the strain-compensated InGaN–AlGaN QW lasers can be attributed to the improved differential gain and reduced threshold carrier density, which leads to the suppression of the nonradiative threshold current density.

It is important to note that recently Shen and co-workers [32] found Auger recombination current density (J_{Auger}) may play important role in thick InGaN–GaN double-heterostructure *active* regions ($\mathrm{d}_{\mathrm{Active}} = 10-77-\mathrm{nm}$) in particular for high carrier density operation. Note that the Auger recombination coefficients (C_{Auger}) in InGaN–GaN QW system still require further studies, due to the large discrepancies from the reported Auger coefficients (C_{Auger}) ranging from $0.9-1\times10^{-32}$ cm^6/s [36] up to $1.4-2\times10^{-30}$ cm^6/s [32]. A significant reduction in threshold carrier density (n_{th}) achievable in the strain-compensated InGaN QW will be crucial for suppressing the $\mathrm{J}_{\mathrm{Auger}}$, as the $\mathrm{J}_{\mathrm{Auger}}$ is proportional to $\sim n_{\mathrm{th}}^3$. The reduction in the threshold carrier density (n_{th}) due to the use of strain-compensated InGaN–AlGaN QW will correspond to ~44.3% reduction in Auger current density at threshold ($J_{\mathrm{th\_Auger}}$).

IX. STRAIN-COMPENSATED InGaN–AlGaN QWS WITH VARIOUS INDIUM CONTENTS (15%, 22% 28%)

The spontaneous emission and optical gain properties for both conventional $In_xGa_{1-x}N$–GaN QW and strain-compensated $In_xGa_{1-x}N$–$Al_{0.2}Ga_{0.8}N$ QW structures are studied and compared for QWs with different indium (In) contents ($x = 15\%$, 22%, and 28%). All the $In_xGa_{1-x}N$ QW active regions studied have thicknesses of 24-Å.

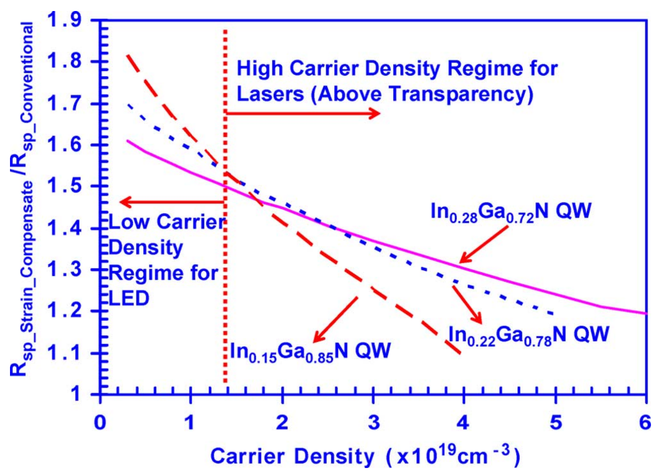

Fig. 15. Ratio of spontaneous emission radiative recombination rate (R_{sp}) for strain-compensated InGaN–AlGaN QW and conventional InGaN–GaN QW as function of carrier density at temperature of 300 K for different Indium contents (15%, 22%, 28%).

Fig. 15 shows the ratio of the spontaneous emission radiative recombination rate for strain-compensated InGaN–AlGaN QW and conventional InGaN–GaN QW for three different In-contents. For the case of QW with lower indium content (15%), the strain-compensated QW exhibited improvement up to ~80% in the low carrier density regime compared to the conventional QW. However, the improvement reduces to ~20% for near threshold condition ($n = 3\times10^{19}$ cm^{-3}). As the indium content in the QW increases from 15% up to 28%, the improvement of the spontaneous emission rate for the strain-compensated QW is reduced from ~80% to ~60% for the low carrier density regime. However, the improvement observed in the high In-content strain-compensated QW is relatively high in the range of ~30%–40% for high carrier density regime of $n = 3-4\times10^{19}$ cm^{-3}.

Fig. 16 shows the comparison of the peak material gain for both conventional and strain-compensated structures for different indium contents. The transparency carrier densities (n_{tr}) for these three cases are relatively similar in the range of $n_{tr} \sim 1.5\times10^{19}$ cm^{-3}. However, both conventional and strain-compensated QW structures with lower In-content (15%) exhibit higher material gain in comparison to those of higher In-contents (22% and 28%) QW structures. The use of strain-compensated QW structures lead to improvement in the peak material gain for all three different indium contents in the QWs. At $n = 3.5\times10^{19}$ cm^{-3}, the strain compensated QWs exhibited improvement of 20%, 27.9%, 33.2% for In-contents of 15%, 22%, and 28%, respectively. The improvement in the material gain is more pronounced in particular for the green-emitting strain-compensated QW ($\mathrm{In-content} = 28\%$), due to the much improved matrix element and carrier confinement in QW from the use of large bandgap AlGaN barriers surrounding the high In-content InGaN QW.

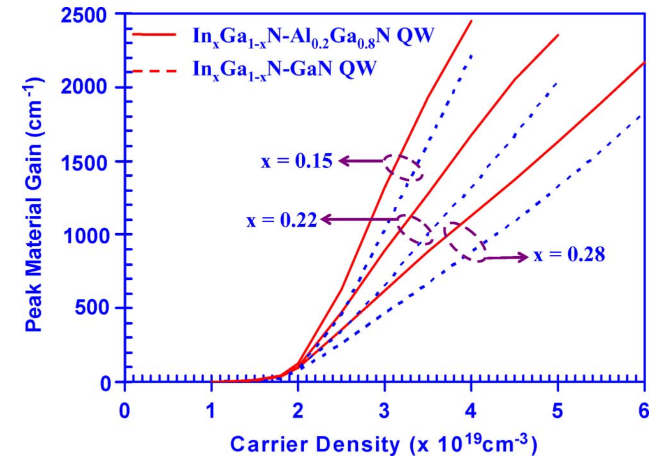

Fig. 16. Peak material gain for strain-compensated InGaN–AlGaN QW and conventional InGaN–GaN QW as function of carrier density at temperature of 300 K for different Indium contents (15%, 22%, 28%).

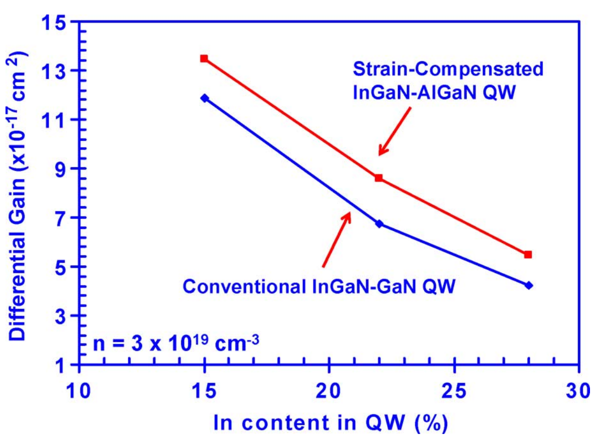

Fig. 17. Differential gain for strain-compensated InGaN–AlGaN QW and conventional InGaN–GaN QW as function of Indium contents (15%, 22%, 28%) at carrier density of 3×10^{19} cm^{-3}.

Fig. 17 shows the differential gain (dg/dn) for both conventional and strain-compensated structures as a function of indium contents (15%, 22%, and 28%) at the carrier density (n) of 3×10^{19} cm^{-3}. As the indium contents in the conventional and strain-compensated QWs increase, the differential gains reduces due to reduced matrix elements. However, the use of strain-compensated QWs leads to increase in the differential gains, in comparison to those of conventional QWs. For the structure with indium content of 15%, the differential gain for strain-compensated QW is $\sim 1.35 \times 10^{-16}$ cm^2, which indicates 13.5% improvement as compared to that of the conventional structure $(\mathrm{dg/dn} = 1.19 \times 10^{-16}$ $\mathrm{cm}^2)$. For the structure with indium content of 28%, the differential gain for the strain-compensated structure $(\mathrm{dg/dn} = 5.5 \times 10^{-17}$ $\mathrm{cm}^2)$ is enhanced by 29.7% compared to the conventional structure $(\mathrm{dg/dn} = 4.24 \times 10^{-17}$ $\mathrm{cm}^2)$.

In Fig. 18, the threshold current densities $(J_{\mathrm{th\_total}} = J_{\mathrm{th\_rad}} + J_{\mathrm{th\_mono}})$ are compared as a function of the indium contents for different monomolecular recombination rates $(A = 6 \times 10^8\ \mathrm{s}^{-1}$, $A = 1 \times 10^9\ \mathrm{s}^{-1}$, and $A = 1.5 \times 10^9\ \mathrm{s}^{-1})$. As the indium content increases from 15%, 22% up to 28%, the threshold current density increases for both conventional

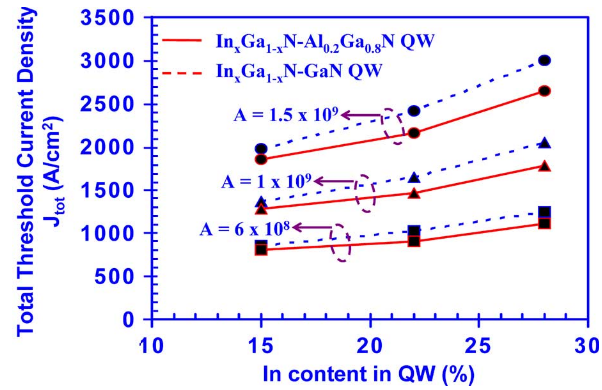

Fig. 18. Threshold current density for strain-compensated InGaN–AlGaN QW and conventional InGaN–GaN QW as function of Indium contents (15%, 22%, 28%) at the threshold gain of 1345 cm^{-1}.

InGaN QW and strain-compensated InGaN–AlGaN QW. The defect nonradiative recombination is a major concern for nitride-based diode lasers, and the use of strain-compensated QW structure will lead to reduction in the threshold current density in particular for the case of QW with large monomolecular recombination rates.

X. Summary

In summary, this paper presents self-consistent comprehensive theoretical and numerical studies on the spontaneous emission, optical gain properties and threshold analysis of strain-compensated InGaN–AlGaN QW as active region for lasers and LEDs with indium-contents ranging from 15%, 22%, and 28%. Due to the tensile AlGaN barriers, the strain-compensated InGaN–AlGaN structure provides a strain-balance structure, which improves the material quality in the active region. The higher band offset of the InGaN–AlGaN QW structure is advantageous for high temperature operation. The calculation of the energy dispersion is based on a 6-band $\boldsymbol{k} \cdot \boldsymbol{p}$ formalism, taking into account the valence band mixing, strain effect, spontaneous and piezoelectric polarization, and carrier screening.

From our analysis, both the spontaneous emission spectra and optical gain of strain-compensated InGaN–AlGaN QW exhibit enhancement in comparison to those of conventional InGaN–GaN QW. The strain-compensated $\mathrm{In_{0.28}Ga_{0.72}N}$–$\mathrm{Al_{0.2}Ga_{0.8}N}$ QW exhibited 50–60% enhancement of the spontaneous emission radiative recombination rate for carrier density for low carrier density regime ($n = 2 \times 10^{18}$ cm^{-3} up to $n = 1 \times 10^{19}$ cm^{-3}), which is advantageous for LED operation. At high carrier density ($n = 1.5 - 6 \times 10^{19}$ cm^{-3}), the spontaneous emission radiative recombination rate of strain-compensated $\mathrm{In_{0.28}Ga_{0.72}N}$–$\mathrm{Al_{0.2}Ga_{0.8}N}$ QW is found to be enhanced by 50% and 30% at transparency and threshold conditions, respectively. The strain-compensated InGaN–AlGaN QW also exhibited improvement of 28% in the peak optical gain, in comparison to that of uncompensated InGaN–GaN QW, resulting in reduction in the threshold carrier density. The peak gain improvement in strain-compensated InGaN-AlGaN QW is a result of its higher differential gain, which is attributed to the larger momentum matrix element of the QW active region [7]–[11], [37]. The reduction in threshold carrier density in the QW is important for suppressing the nonradiative recombination current density ($\mathrm{J_{mono}} \sim n_{\mathrm{th}}, \mathrm{J_{Auger}} \sim n_{\mathrm{th}}^3$), which in turn will lead to a reduction in the threshold current density of the QW lasers. The threshold analysis, taking into account the monomolecular recombination process as the only nonradiative process, indicates that a reduction of 12% in the threshold current density for the strain-compensated InGaN–AlGaN QW lasers. The reduction in the threshold carrier density (n_{th}) in the strain-compensated InGaN–AlGaN QW will correspond to ~44.3% reduction in Auger current density at threshold ($J_{\mathrm{th\_Auger}}$). As comparison purpose, the observed improvements in strain-compensated InGaN–AlGaN QWs are in the same range with those observed for the strain-compensated InGaAsN–GaAsP QW systems, where ~15–30% increase in peak optical gain [38] and 20% reduction in threshold current density [20] were achieved over the uncompensated InGaAsN–GaAs QW.

REFERENCES

[1] S. Nakamura, M. Senoh, N. Iwasa, S. Nagahama, T. Yamada, and T. Mukai, "Superbright green InGaN single-quantum-well-structure light-emitting diodes," *Jpn. J. Appl. Phys.*, vol. 34, pp. L1332–L1335, Oct. 1995.

[2] J. Zhang, J. Yang, G. Simin, M. Shatalov, M. A. Khan, M. S. Shur, and R. Gaska, "Enhanced luminescence in InGaN multiple quantum wells with quaternary AlInGaN barriers," *Appl. Phys. Lett.*, vol. 77, pp. 2668–2670, Oct. 2000.

[3] X. Guo, Y. L. Li, and E. F. Schubert, "Efficiency of GaN/InGaN light-emitting diodes with interdigitated mesa geometry," *Appl. Phys. Lett.*, vol. 79, pp. 1936–1938, Sep. 2001.

[4] B. Witzigmann, V. Laino, M. Luisier, U. T. Schwarz, G. Feicht, W. Wegscheider, K. Engl, M. Furitsch, A. Leber, A. Lell, and V. Härle, "Microscopic analysis of optical gain in InGaN/GaN quantum wells," *Appl. Phys. Lett.*, vol. 88, Jan. 2006, Art. 021104.

[5] I. H. Brown, P. Blood, P. M. Smowton, J. D. Thomson, S. M. Olaizola, A. M. Fox, P. J. Parbrook, and W. W. Chow, "Time evolution of the screening of piezoelectric fields in InGaN quantum wells," *IEEE J. Quantum Electron.*, vol. 42, no. 12, pp. 1202–1208, Dec. 2006.

[6] R. M. Farrell, D. F. Feezell, M. C. Schmidt, D. A. Haeger, K. M. Kelchner, K. Iso, H. Yamada, M. Saito, K. Fujito, D. A. Cohen, J. S. Speck, S. P. DenBaars, and S. Nakamura, "Continuous-wave operation of AlGaN-cladding-free nonpolar m-plane InGaN/GaN laser diodes," *Jpn. J. Appl. Phys.*, vol. 46, pp. L761–L763, Aug. 2007.

[7] J. Park and Y. Kawakami, "Photoluminescence property of InGaN single quantum well with embedded AlGaN δ layer," *Appl. Phys. Lett.*, vol. 88, May 2006, Art. 202107.

[8] S. H. Park, J. Park, and E. Yoon, "Optical gain in InGaN/GaN quantum well structures with embedded AlGaN delta layer," *Appl. Phys. Lett.*, vol. 90, Jan. 2007, Art. 023508.

[9] R. A. Arif, Y. K. Ee, and N. Tansu, "Polarization engineering via staggered InGaN quantum wells for radiative efficiency enhancement of light emitting diodes emitting," *Appl. Phys. Lett.*, vol. 91, no. 9, Aug. 2007, Art. 091110.

[10] R. A. Arif, H. Zhao, and N. Tansu, "Spontaneous emission and characteristics of staggered InGaN quantum-well light-emitting diodes," *IEEE J. Quantum Electron.*, vol. 44, no. 6, pp. 573–580, Jun. 2008.

[11] R. A. Arif, H. Zhao, and N. Tansu, "Type-II InGaN-GaNAs quantum wells active regions for lasers applications," *Appl. Phys. Lett.*, vol. 92, no. 1, Jan. 2008, Art. No. 011104.

[12] H. Zhao, R. A. Arif, Y. K. Ee, and N. Tansu, "Optical gain analysis of strain-compensated InGaN-AlGaN quantum well active regions for lasers emitting at 420–500 nm," *Opt. Quantum Electron.*, vol. 40, no. 5–6, pp. 301–306, Apr. 20078.

[13] H. Zhao, R. A. Arif, Y. K. Ee, and N. Tansu, "Optical gain and spontaneous emission of strain-compensated InGaN-AlGaN quantum wells including carrier screening effect," in *Proc. SPIE Photonics West 2008, Physics and Simulation of Optoelectronics Devices XVI*, San Jose, CA, Jan. 2008, vol. 6889, p. 688903.

[14] N. Tansu, N. J. Kirsch, and L. J. Mawst, "Low-threshold-current-density 1300-nm dilute-nitride quantum well lasers," *Appl. Phys. Lett.*, vol. 81, pp. 2523–2525, Sep. 2002.

[15] N. Tansu, J. Y. Yeh, and L. J. Mawst, "Extremely low threshold-current-density InGaAs quantum well lasers with emission wavelength of 1215–1233 nm," *Appl. Phys. Lett.*, vol. 82, pp. 4038–4040, Jun. 2003.

[16] N. Tansu, J. Y. Yeh, and L. J. Mawst, "Physics and characteristics of 1200-nm InGaAs and 1300–1400 nm InGaAsN quantum-well lasers by metalorganic chemical vapor deposition," *IOP J. Physics: Condens. Matter Phys.*, vol. 16, pp. S3277–S3318, Aug. 2004.

[17] S. J. Chang, C. H. Kuo, Y. K. Su, L. W. Wu, J. K. Sheu, T. C. Wen, W. C. Lai, J. F. Chen, and J. M. Tsai, "400-nm InGaN-GaN and InGaN-AlGaN multiquantum well light-emitting diodes," *IEEE J. Sel. Topics Quantum Electron.*, vol. 8, no. 4, pp. 744–748, Jul./Aug. 2002.

[18] N. Tansu and L. J. Mawst, "Current injection efficiency of 1300-nm InGaAsN quantum-well lasers," *J. Appl. Phys.*, vol. 97, pp. 2523–2525, Mar. 2005, Art. No. 054502.

[19] T. Fukunaga, M. Wada, and T. Hayakawa, "Reliable operation of strain-compensated 1.06 μm InGaAs/InGaAsP/GaAs single quantum well lasers," *Appl. Phys. Lett.*, vol. 69, pp. 248–250, Jul. 1996.

[20] N. Tansu, J. Y. Yeh, and L. J. Mawst, "Experimental evidence of carrier leakage in InGaAsN quantum well lasers," *Appl. Phys. Lett.*, vol. 83, pp. 2112–2114, Sep. 2003.

[21] S. L. Chuang and C. S. Chang, "$k \cdot \mathrm{p}$ method for strained wurtzite semiconductors," *Phys. Rev. B.*, vol. 54, pp. 2491–2504, Jul. 1996.

[22] S. L. Chuang, "Optical gain of strained wurtzite GaN quantum-well lasers," *IEEE J. Quantum Electron.*, vol. 32, no. 10, pp. 1791–1800, Oct. 1996.

[23] S. H. Park and S. L. Chuang, "Many-body optical gain of wurtzite GaN-based quantum-well lasers and comparison with experiment," *Appl. Phys. Lett.*, vol. 72, no. 3, pp. 287–289, Jan. 1998.

[24] F. Bernardini and V. Fiorentini, "Spontaneous versus piezoelectric polarization in III–V Nitrides: Conceptual aspects and practical consequences," *Phys. Stat. Sol. (b)*, vol. 216, pp. 391–398, Nov. 1999.

[25] O. Ambacher, J. Majewski, C. Miskys, A. Link, M. Hermann, M. Eickhoff, M. Stutzmann, F. Bernardini, V. Fiorentini, V. Tilak, W. J. Schaff, and L. F. Eastman, "Pyroelectric properties of Al(In)GaN/GaN hetero- and quantum well structures," *J. Phys.: Condens. Matter*, vol. 14, pp. 3399–3434, Mar. 2002.

[26] W. W. Chow and M. Kneissl, "Laser gain properties of AlGaN quantum wells," *J. Appl. Phys.*, vol. 98, Dec. 2005, Art. 114502.

[27] S. L. Chuang, *Physics of Optoelectronics Devices*. New York: Wiley, 1995, ch. 4 and 9.

[28] S. L. Chuang and C. S. Chang, "A band-structure model of strained quantum-well wurtzite semiconductors," *Semicond. Sci. Technol.*, vol. 12, pp. 252–263, 1997.

[29] I. Vurgaftman and J. R. Meyer, *Nitride Semiconductor Devices*, J. Piprek, Ed. New York: Wiley, 2007, ch. 2.

[30] I. Vurgaftman and J. R. Meyer, "Band parameters for nitrogen-containing semiconductors," *J. Appl. Phys.*, vol. 94, pp. 3675–3696, Sep. 2003.

[31] N. F. Gardner, G. O. Muller, Y. C. Shen, G. Chen, S. Watanabe, W. Gotz, and M. R. Krames, "Blue-emitting InGaN-GaN double-heterostructure light emitting diodes reaching maximum quantum efficiency above 200 A/cm^2," *Appl. Phys. Lett.*, vol. 91, Dec. 2007, Art. 243506.

[32] Y. C. Shen, G. O. Mueller, S. Watanabe, N. F. Gardner, A. Munkholm, and M. R. Krames, "Auger recombination in InGaN measured by photoluminescence," *Appl. Phys. Lett.*, vol. 91, Oct. 2007, Art. 141101.

[33] P. G. Eliseev, M. Osinski, H. Li, and I. V. Akimova, "Recombination balance in green-light-emitting GaN/InGaN/AlGaN quantum wells," *Appl. Phys. Lett.*, vol. 75, pp. 3838–3840, Dec. 1999.

[34] M. Röwe, P. Michler, J. Gutowski, V. Kümmler, A. Lell, and V. Härle, "Influence of the carrier density on the optical gain and refractive index change in InGaN laser structures," *Phys. Stat. Solidi (A)*, vol. 200, pp. 135–138, Sep. 2003.

[35] H. Y. Ryu, K. H. Ha, S. N. Lee, T. Jang, J. K. Son, H. S. Paek, Y. J. Sung, H. K. Kim, K. S. Kim, O. H. Nam, Y. J. Park, and J. I. Shim, "Highly stable temperature characteristics of InGaN blue laser diodes," *IEEE Photon. Technol. Lett.*, vol. 19, no. 11, pp. 1717–1719, Nov. 2007.

[36] J. Hader, J. V. Moloney, A. Thranhardt, and S. W. Koch, "Interband transitions in InGaN quantum wells," in *Nitride Semiconductor Devices*, J. Piprek, Ed. Weinheim, Germany: Wiley-VCH, 2007, ch. 7, p. 164.

[37] H. Zhao, R. A. Arif, and N. Tansu, “Self consistent analysis of Type-II ’W’ InGaN-GaNAs quantum well lasers,” *J. Appl. Phys.*, vol. 104(5), Sep. 2008, Art. 043104.

[38] S. B. Healy and E. P. O’Reilly, “Influence of electrostatic confinement on optical gain in GaInNAs quantum-well lasers,” *IEEE J. Quantum Electron.*, vol. 42, no. 6, pp. 608–615, Jun. 2006.

Hongping Zhao received the B.S. degree in physics from Nanjing Normal University, Nanjing, China, in 2003 and the M.S. degree in electrical engineering from Southeast University, China, in 2005. She has been pursuing the Ph.D degree in the Electrical and Computer Engineering Department at Lehigh University, Bethlehem, PA, since January 2007.

Her research areas cover device physics, epitaxial growth, and fabrication of semiconductor optoelectronics devices based on semiconductor nanostructures. Her current research works include fundamental studies and approaches to improve gain and spontaneous emission of visible gain media based on III–Nitride semiconductors for high performance lasers, and MOCVD exitaxy of InN material for quantum dots and solar cell applications. She has also published more than 30 refereed journal and conference publications

Ms. Zhao is the recipient of the 2008 SPIE Educational Scholarship and Sherman Fairchild Fellowship on Solid State Studies.

Ronald A. Arif received the B.S. degree in materials engineering from Nanyang Technological University, Singapore, in May 2002, the M.S. degree in electrical engineering in 2005 from Lehigh University, Bethlehem, PA, where he is currently pursuing the Ph.D. degree in electrical engineering.

He was a Process Engineer with Agilent Technologies, Singapore from 2002 to 2003. His research works include fundamental studies and novel approaches to improve radiative efficiency of visible gain media based on III–Nitride semiconductor nanostructures for high efficiency LEDs and lasers, in particular for solid state lighting. He has also published more than 45 refereed journal and conference publications.

Yik-Khoon Ee received the B.S. degree in electrical and electronic engineering from Nanyang Technological University, Singapore, in 2003 and the M.S. degree in 2007 from Lehigh University, Bethlehem, PA, where he is currently pursuing the Ph.D. degree in the Department of Electrical and Computer Engineering.

Subsequently, he worked in Denselight Semiconductors and Agilent Technologies. His research works are in the field of semiconductor optoelectronics, MOCVD epitaxy, device fabrication of III–Nitride LEDs. His research focus also includes the growth of and modeling of InGaN quantum dots, and he has more than 40 refereed journal and conference publications to his credit.

Nelson Tansu was born in 1977. He received the B.S. degree in applied mathematics, electrical engineering, and physics (highest distinction) and the Ph.D. degree in electrical engineering from the University of Wisconsin-Madison in 1998 and 2003, respectively.

Since July 2003, he has been an Assistant Professor in the Department of Electrical and Computer Engineering (ECE) and the Center for Optical Technologies (COT) at Lehigh University, Bethlehem, PA, since April 2007. He has been appointed as the Peter C. Rossin Assistant Professor of Electrical and Computer Engineering at Lehigh University. His research works cover the theoretical and experimental aspects of the physics of semiconductor optoelectronics materials and devices, the physics of low-dimensional semiconductor (nanostructure), and MOCVD epitaxy and device fabrications of III–Nitride and III–V–Nitride semiconductor optoelectronics devices on GaAs, InP, and GaN substrates. His teaching interests are in the areas of optoelectronics and photonics, semiconductor physics, applied quantum mechanics, and engineering electromagnetism. He has published widely in numerous (total > 147) refereed international journal and conference publications and he also currently holds several U.S. patents.

Dr. Tansu was a recipient of the Bohn Scholarship, the WARF Graduate University Fellowship, the Vilas Graduate University Fellowship, and the Graduate Dissertator Travel Funding Award, the 2003 Harold A. Peterson ECE Best Research Award (First Prize) at the University of Wisconsin-Madison. He is also a recipient of the 2008 Libsch Early Career Research Award from Lehigh University. He had served several times as a panel member for U.S. National Science Foundation, U.S. Department of Defense, and other agencies in the U.S. and abroad. He has also given numerous lectures, seminars, and invited talks in universities, research institutions, and conferences in the U.S., Canada, Europe, and Asia. He is also the Primary Guest Editor for IEEE JOURNAL OF SELECTED TOPICS IN QUANTUM ELECTRONICS—SPECIAL ISSUE ON SOLID STATE LIGHTING in 2008–2009.